Nano Energy (2014) **10**, 295–304

Available online at www.sciencedirect.com

ScienceDirect

journal homepage: www.elsevier.com/locate/nanoenergy

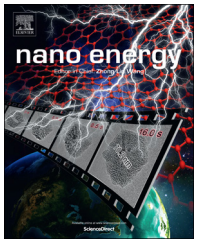

RAPID COMMUNICATION

In situ generated FeF_3 in homogeneous iron matrix toward high-performance cathode material for sodium-ion batteries

De-long Ma[b,c], Heng-guo Wang[b], Yang Li[a], Dan Xu[b], Shuang Yuan[b,c], Xiao-lei Huang[b], Xin-bo Zhang[b], Yu Zhang[a,*]

[a]*Key Laboratory of Bio-Inspired Smart Interfacial Science and Technology of Ministry of Education, School of Chemistry and Environment, Beihang University, Beijing 100191, PR China*
[b]*State Key Laboratory of Rare Earth Resource Utilization, Changchun Institute of Applied Chemistry, Chinese Academy of Sciences, Changchun 130022, PR China*
[c]*Key Laboratory of Automobile Materials, Ministry of Education and School of Materials Science and Engineering, Jilin University, Changchun 130012, PR China*

Received 12 September 2014; received in revised form 5 October 2014; accepted 6 October 2014
Available online 16 October 2014

KEYWORDS
Na-ion batteries;
FeF_3;
Cathode;
High performance

Abstract
A strategy for enabling highly insulated FeF_3 as high performance cathode materials for NIBs is proposed and realized, through constructing metallic Fe and reduced graphene oxide (RGO) double enhancement conducting matrix, wherein both the metallic Fe and active FeF_3 are *in situ* electrochemically generated from one FeF_2 grain (as precursor of FeF_3) to ensure their desired homogenous and intimate contact. The efficacy of this concept is demonstrated by the superior electrochemical performance of the generated FeF_3-Fe-RGO composite including high capacity of 150 mA h g^{-1} at a current density of 50 mA g^{-1}, good cycle stability, and high power capability at room temperature, which could be reasonably attributed to homogeneous conductive matrix composed of metallic Fe and RGO in the composite and especially their ideal contact with the active FeF_3 component. The strategy is simple yet very effective and also because of its versatility, it may be easily extended to other next generation high-capacity electrode materials while with low electrical conductivity.
© 2014 Published by Elsevier Ltd.

*Corresponding author.
E-mail address: jade@buaa.edu.cn (Y. Zhang).

http://dx.doi.org/10.1016/j.nanoen.2014.10.004
2211-2855/© 2014 Published by Elsevier Ltd.

Introduction

The past two decades have witnessed Li-ion batteries (LIBs) capture the portable electronic markets [1-8]. However, we shall always be prepared for the exhaustion of limited and unevenly distributed lithium resources. In response, room-temperature sodium-ion batteries (NIBs) have aroused interest recently as an attractive alternative technology because sodium resources are practically inexhaustible and ubiquitous [9-12]. However, due to the intrinsically much larger ionic radius of sodium ion than that of lithium ion, there is still only limited number of potential cathode materials for NIBs [13-21]. The development of suitable cathode materials is urgently desirable but remains a challenging issue.

Metal fluorides, as one of the most important family of functional inorganic materials, have numerous applications in the field of catalysts, optical devices, and magnetic materials as well as potential cathode materials in LIBs, due to their high theoretical capacity, low cost, abundant sources, low toxicity, and high safety, which are crucial for large-scale electrochemical energy storage [22-27]. In addition, they are better choice for Li/Na-polymer batteries which use metal Li/Na as anode. Because most of metal fluorides (such as FeF_2, FeF_3, and NiF_2) don't contain Li/Na. Unfortunately, metal fluorides are notorious for their intrinsically poor electronic conductivity due to the large band gap [*e.g.* 5.96 eV for metal trifluoride (FeF_3)] induced by the highly ionic character of the metal-halogen bond, resulting in a very low actual capacity and fast capacity fading [28-31], which had almost kept them away from the radar screen in the search for improved electrodes materials for LIBs, to say nothing of NIBs. To overcome this problem, one possible method is addition of conductive additives such as carbon materials (graphite, carbon black, activated carbon, etc.), metal oxides and metal sulfides (V_2O_5, MoO_3, MoS_2, etc.) [32-34]. Despite significant improvements have been achieved, the obtained performances are still far from satisfying, because the desired intimate and homogeneous conducting matrix between active metal fluorides particles and conductive additives, which is of critical importance for enabling highly insulated FeF_3 as feasible cathode materials for NIBs, cannot be fully achieved by adding (*e.g.* ball milling) pre-generated (*ex situ*) conductive additives. Therefore, it is coveted but still a big challenge to further significantly enhance the electronic conductivity and thus the electrochemical performance of metal fluorides in NIBs.

Herein, as a proof-of-concept experiment, we propose and realize a strategy for enabling highly insulated FeF_3 as high performance cathode materials for NIBs through constructing metallic Fe and reduced graphene oxide (RGO) double enhancement conducting matrix, wherein both the metallic Fe and active FeF_3 are *in situ* electrochemically generated from one FeF_2 grain (as precursor of FeF_3) to ensure their desired homogenous and intimate contact. The efficacy of this concept is demonstrated by the superior electrochemical performance of the generated FeF_3-Fe-RGO composite including high capacity of 150 mA h g^{-1} at a current density of 50 mA g^{-1}, good cycle stability, and high power capability at room temperature, which could be reasonably attributed to homogeneous conductive matrix composed of metallic Fe and RGO in the composite and especially their ideal contact with the active FeF_3 component. The strategy is simple yet very effective and also because of its versatility, it may be easily extended to other next generation high-capacity electrode materials while with low electrical conductivity.

Experimental methods

Synthesis of α-$FeF_3 \cdot 3H_2O$

The fabrication process was performed using Teflon or plastic wares. First, a certain amount of $FeCl_3$ solution was added to the 10% excess mass of stoichiometric NaOH solution with violently stirring for 30 min and the precipitation was washed and separated by centrifugation. Second, the above precipitation was added to excessive HF solution with continued stirring for 12 h at 50 °C, and then the solution was frozen in refrigerator. After that, the α-$FeF_3 \cdot 3H_2O$ was obtained by freeze drying.

Synthesis of graphene oxide (GO)

GO was prepared by a modified Hummers method. Typically, 0.375 g of graphite powder and 2.25 g of $KMnO_4$ were added to concentrated H_2SO_4/H_3PO_4 (45:5 mL). After stirring 24 h at 50 °C, the reaction was cooled to room temperature and poured onto ice (200 mL) with 30% H_2O_2 (3 mL). Then the mixture was centrifuged (8000 rpm for 5 min). The remaining solid material was washed with 200 ml of 30% HCl for at least three times, and 200 ml of water for three times. Finally, GO was dispersed in water up to the concentration of 1 mg mL^{-1}.

Synthesis of FeF_2-RGO and $FeF_3 \cdot 0.33H_2O$

Precursor solutions were obtained by desired amount of $FeF_3 \cdot 3H_2O$ into water at room temperature to achieve the desired concentration (230 mg mL^{-1}). Then, 170 μL FeF_3 solution was added into 10 mL GO suspension (1 mg mL^{-1}) and stirred for 20 min at room temperature. After that, the mixed suspension was frozen in liquid N_2 and the precursor $FeF_3 \cdot 3H_2O$-GO was obtained by freeze drying. Finally, FeF_2-RGO and $FeF_3 \cdot 0.33H_2O$ composites were prepared by thermal dehydration and reduction of the as-synthesized $FeF_3 \cdot 3H_2O$-GO precursor in an inert atmosphere using a tube furnace equipped with gas flow controls. Briefly, a large alumina boat containing ~100 mg $FeF_3 \cdot 3H_2O$-GO precursor were placed at the center of the tube furnace. The tube was first slowly evacuated and flushed three times with N_2 gas and then the precursor were kept under vacuum (~40 mTorr) at 60 °C to for 120 min to dry completely. Then under a flowing argon gas at a rate of 200 sccm, the furnace temperature was slowly ramped from 50 °C to 220 °C or 350 °C (~2 °C min^{-1}) and held at 220 °C for 3 h to get $FeF_3 \cdot 0.33H_2O$-RGO, 350 °C for 90 min to get FeF_2-RGO.

Synthesis of B-FeF_2, B-FeF_3 and B-FeF_3-Fe

B-FeF_2, B-FeF_3, and B-FeF_3-Fe were obtained by ball milling the commercial purchased samples for 3 h.

Substitution of metallic Fe with Ag

After 50 discharge–charge cycles, the obtained electrode materials were immersed in acetonitrile for 12 h. And then they were washed with acetonitrile and ethanol for at least five times. Finally the electrode materials were immersed in ethanol solution of $AgNO_3$ for 12 h at dark place and were washed with ethanol for several times before using.

Material characterization

The morphology and crystalline structure of as-obtained samples were characterized with scanning electron microscopy (SEM Hitachi S-4800) and transmission electron microscope (TEM) recorded on a Tecnai G2 operating at 200 kV. X-ray diffraction (XRD) patterns were recorded on Bruker D8 Focus Powder X-ray diffractometer with Cu *K*α radiation. Thermogravimetric (TG) analysis was performed on a NETZSCH STA 449 F3 Simultaneous TGA-DSC Instrument. X-ray photoelectron spectroscopy (XPS) analysis was carried on an ESCALAB MK II X-ray photoelectron spectrometer. Raman spectra were collected using a micro-Raman spectrometer (Renishaw) with a laser of 532 nm wavelength.

Electrochemical evaluation

The electrodes were prepared by mixing active materials (70 wt% for FeF_2-RGO and $FeF_3 \cdot 0.33H_2O$-RGO, and 50 wt% for others), acetylene black (20 wt% for FeF_2-RGO and $FeF_3 \cdot 0.33H_2O$-RGO, and 35 wt% for others), and polyvinylidene fluoride (PVDF, 10 wt% for FeF_2-RGO and $FeF_3 \cdot 0.33H_2O$-RGO, and 15 wt% for others) in *N*-methyl-2-pyrrolidone (NMP). After the above slurries were uniformly spread onto aluminum foil, the electrodes were dried at 80 °C in vacuum for 12 h. Then the electrodes were pressed and cut into disks before transferring into an Argon-filled glove box. Coin cells (CR2025) were laboratory-assembled using Na metal as the counter electrode, Celgard 2400 membrane as the separator and $NaPF_6$ (1 M) in ethylene carbonate/diethyl carbonate (EC/DEC, 1:1 wt%) as the electrolyte. The galvanostatic charge-discharge tests were carried out on a Land Battery Measurement System (Land, China). Cyclic voltammetry (CV) was performed using a VMP3 Electrochemical Workstation (Biologic Inc.).

Results and discussion

A brief summary of the synthesis procedure of FeF_3-Fe-RGO composite is schematically presented in Figure 1. Briefly, the FeF_2-RGO precursor ($FeF_3 \cdot 3H_2O$-GO) is first synthesized through a simple and high yield freeze drying method, inspired by a natural principle in sea ice [35,36]. That is, the salt ($FeF_3 \cdot 3H_2O$) in the solution is expelled from the forming ice and nucleates and grows along the surface of GO, wherein the GO is entrapped within channels between the ice crystals to avoid the agglomeration of GO during vacuum drying. Then, the FeF_2-RGO composite is obtained after heat treatment under nitrogen (N_2) atmosphere, wherein the GO and FeF_3 (by carbon of GO) are reduced simultaneously. Finally, the desired FeF_3-Fe-RGO composite is *in situ* generated through an electrochemical activation process.

X-ray diffraction (XRD) analysis is performed to investigate the crystal phase of the synthesized samples. All the diffraction peaks of the fabricated sample after freeze drying could be indexed to α-$FeF_3 \cdot 3H_2O$ [37] (majority, space group *R*3*m*, a=9.5135 Å, c=4.7882 Å) and FeF_3 (minority, JCPDS no. 84-1101) (Figure 2a). It is found that, after heat treatment (350 °C for 90 min) under N_2 atmosphere, both α-$FeF_3 \cdot 3H_2O$ and FeF_3 are reduced to FeF_2 by the carbon of RGO (Figure 2a). It should be note that diffraction peaks of FeF_3 can be observed in the XRD pattern after heat treatment. However, compared with FeF_2, it only takes a small portion, which will not affect the performance of FeF_2. Note that the absence of peaks for GO or RGO could be attributed to its covering by $FeF_3 \cdot 3H_2O$ or FeF_2 and thus no serious restacking of GO or RGO, which is consistent with the morphology results (vide infra). X-ray photoelectron spectroscopy (XPS) is employed to further confirm the formation of FeF_2-RGO (Figure S1). Figure S1a shows one peak positioned at 710.5 eV, suggesting +2 oxidation state of iron [38] and the formation of FeF_2. On the other hand, as shown in Fig. S1b, after heat treatment, the peak at 284.5 eV (C-C) becomes much higher than the others (C=O and C-O), indicating that oxygen-containing functional groups in GO are effectively removed during the heat treatment under N_2 atmosphere [39-45]. In addition, the Raman spectrum (Figure S2) shows that the peak intensity ratio of *D* to *G* (I_D/I_G) changes from 0.8 to 0.98 after heat treatment, indicating that GO is reduced and subsequently more defects are formed [39,40], which is consistent with the above XPS result. Thermogravimetric analysis (TG) is then used to determine the amount of FeF_2 in the obtained FeF_2-RGO composite (Figure 2b). It is found that, during heat treatment to 600 °C in air, 25% of the total mass is lost.

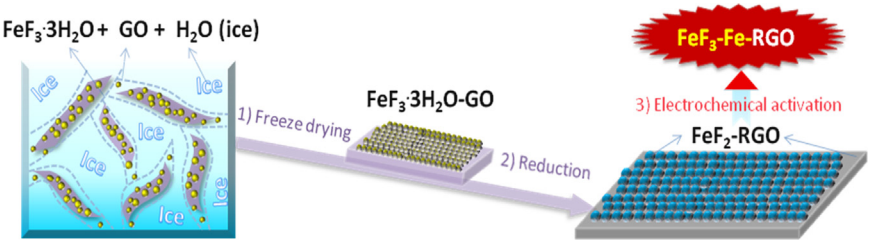

Fig. 1 Schematic representation of the synthesis of FeF_3-Fe-RGO.

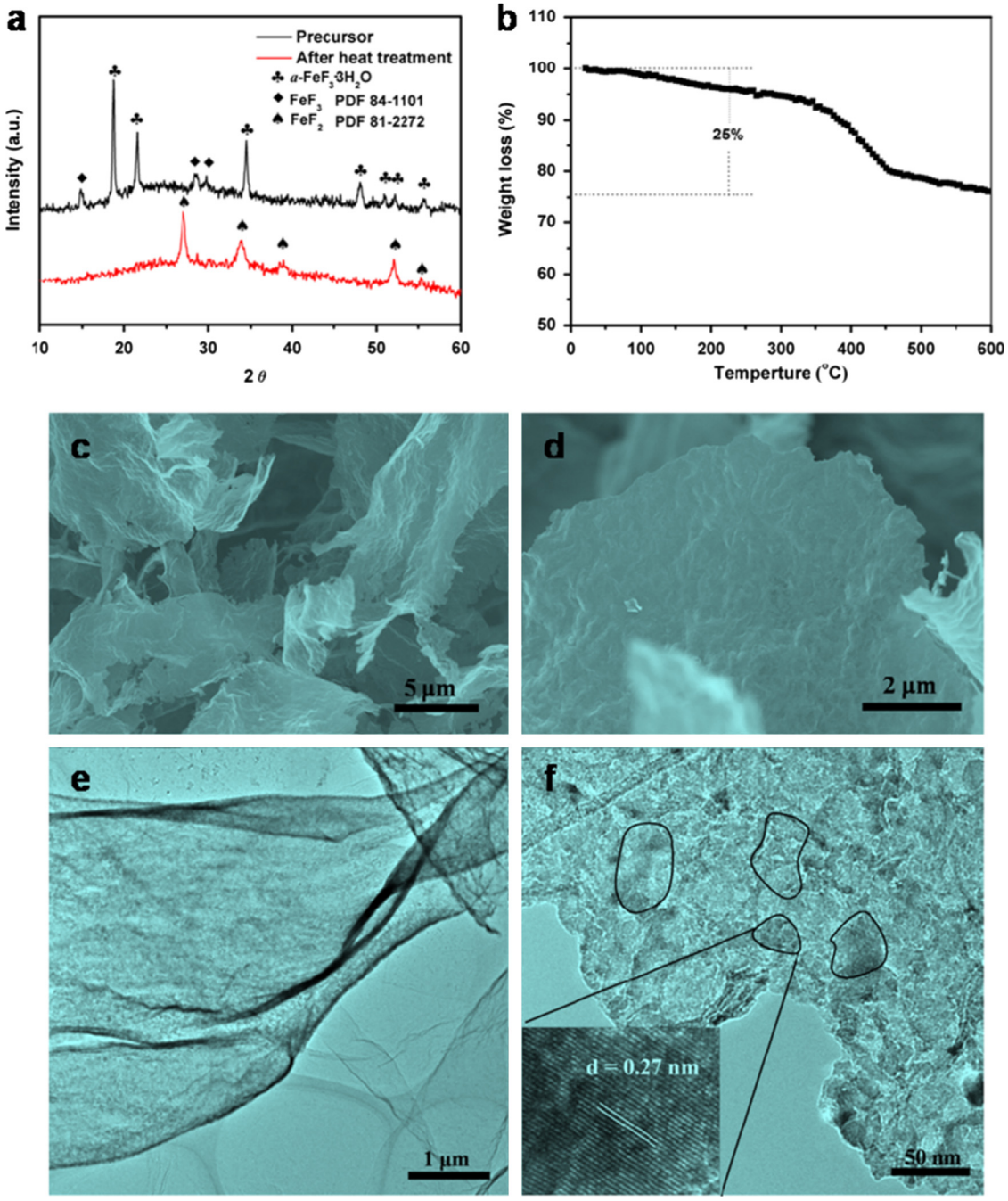

Fig. 2 (a) XRD patterns of the as-prepared sample before and after heat treatment (350 °C for 90 min). (b) TG curves of the FeF_2-RGO measured from 0 to 600 °C at a heating rate of 10 °C min^{-1} in air. ((c) and (d)) SEM and ((e) and (f)) TEM images of the FeF_2-RGO composite. The inset of Fig. 2f shows the image of high-resolution TEM. The *d*-spacing of 0.27 nm corresponds to the (1 0 1) plane of FeF_2.

According to the heating reaction equation ($4FeF_2+4H_2O+O_2=2Fe_2O_3+8HF$) [46], it can be calculated that FeF_2 comprises 88% of the composite mass (refer to Figure S8 for detailed calculation method; FeF_3/Fe/RGO=5.5/1.8/1). The morphology and structure of as-prepared FeF_2-RGO sample are investigated by scanning electron microscopy (SEM) and transmission electron microscopy (TEM). Interestingly, it is found that the FeF_2-RGO inherits the large area sheet structure of GO and there are no large particles aggregation, which is further confirmed by the TEM images (Figure 2e and f), wherein the FeF_2 is found to be homogeneously distributed on the RGO sheet with sheet like structure (ca. 20–40 nm in diameter). The *d*-spacing in the high-resolution TEM is measured to be 0.27 nm (inset of Figure 2f), which corresponds to the spacing of the (1 0 1) plane of FeF_2.

Coin cells with metallic Na counter electrode are assembled and galvanostatic discharge–charge technique is employed to evaluate the electrochemical performance at room temperature. It should be noted that an

electrochemical activation method is advisedly employed to *in situ* generate active FeF_3 and conductive Fe from FeF_2. To this end, the first discharge–charge cycle of all the samples is tested at a current density of 20 mA g^{-1} between 0.8 and 4.5 V, while the successive cycles are tested at different current densities between 1.5 and 4.5 V. As shown in Fig. 3a, the first discharge capacity achieves as high as 340 mA h g^{-1}. Note that the capacity is calculated based on the weight of composite materials, not just FeF_2. Clearly, the discharge profile can be divided into two parts: the initially sloped area between 2.7 and 1.4 V might be stemmed from the Na^+ stored among the grain boundaries [30], absorbed on the surface of RGO, and reacted with a small amount of surface FeF_2 (with low polarization). This is followed by a reaction plateau at about 1.1 V, which is due to the electrochemical decomposition of FeF_2 to NaF and metallic Fe through a conversion reaction. Subsequently, the charging profile can also be divided into two parts with a reaction plateau below 3.0 V (formation of FeF_2 and small amount of FeF_3 with low polarization) and a sloped area from 3.0 to 4.5 V (oxidation of FeF_2 to FeF_3), which is consistent with the XRD and XPS results (vide infra). It

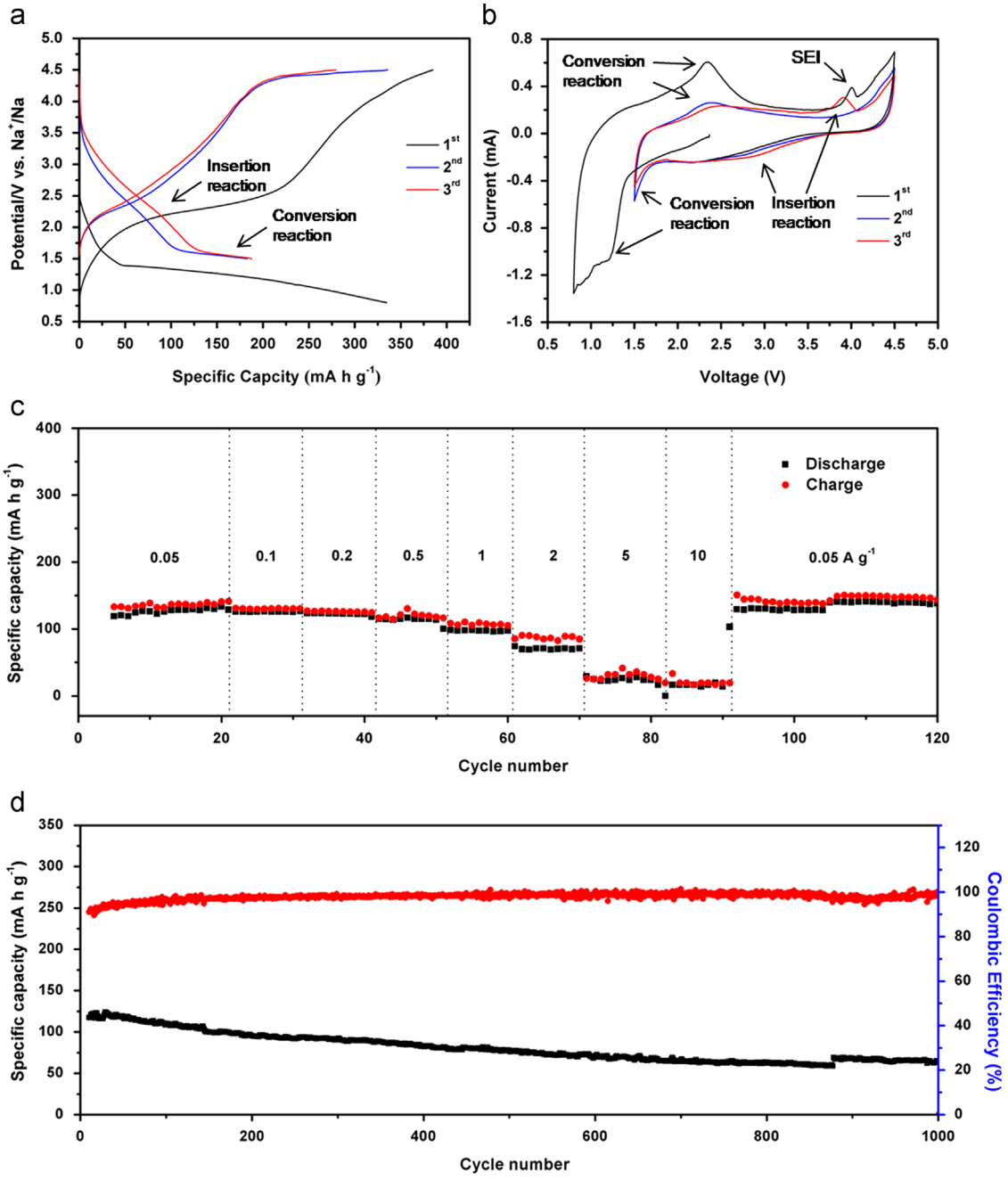

Fig. 3 Electrochemical activation of the FeF_2-RGO composite for *in situ* generation of the FeF_3-Fe-RGO composite (a) charge-discharge curves, (b) cyclic voltammetry profiles, electrochemical performance of the above *in situ* generated FeF_3-Fe-RGO composite (c) rate performance, and (d) cycling stability (current density: 100 mA g^{-1}).

should be noted that formation of SEI could also be responsible for the overcharge at high potential [47]. From the viewpoint of practical application as cathode and thus to avoid the low potential conversion reaction of above *in situ* generated FeF_3, the potential of discharge is limited to 1.5 V from the second cycle. Similarly, it is found that the second discharge profile can also be divided into two parts: the initially sloped area between 3.8 and 1.7 V derives from the interaction of Na^+ into the above *in situ* generated FeF_3 during the first cycle, while the reaction plateau at ca. 1.5 V is due to the conversion reaction of residual FeF_2 with Na^+. The second charge is similar to that of the first charge process except that the potential is increased which could be related to the deintercalation of Na^+ from $NaFeF_3$. In the third discharge curve, the slope area becomes larger while the low potential plateau area significantly decreases, indicating the amount the FeF_3 are increased at the cost of reducing of the FeF_2. In the third charge profile, the plateau at ca. 4.3 V becomes smaller, indicating the high potential required to oxidation of FeF_2 to FeF_3 decreases, because the amount of the residual FeF_2 significantly decreases during the first and second electrochemical activation processes, which might also indicates that the formed SEI, if any, is stable (avoiding continuously formation of SEI layer). Fig. 3c shows the rate capability of above *in situ* generated FeF_3-Fe-RGO composite when current densities are increased from 0.05 to 10 A g^{-1}. It is found that the FeF_3-Fe-RGO composite can deliver a capacity of 100 mA h g^{-1} even at a current density of 0.5 A g^{-1}. Even under a high current density of 2 A g^{-1}, it can also deliver a capacity of 60 mA h g^{-1}. All these results show that the FeF_3-Fe-RGO composite holds superior rate capability. It should be noted that the capacity can be recovered when the rate is reduced to 0.05 A g^{-1}, indicating good stability of the FeF_3-Fe-RGO composite during the high rate discharge-charge cycles, which can also be supported by the long-term cycling test. As shown in Fig. 3d, even after 1000 cycles under a current density of 100 mA g^{-1}, the FeF_3-Fe-RGO composite still retain a reversible capacity of about 70 mA h g^{-1} and the columbic efficiency is still as high as 100%, showing good cycling stability.

To further understand the electrochemical activation process and Na^+ storage mechanism of FeF_2-RGO toward *in situ* generated FeF_3-Fe-RGO composite, the structural evolution of FeF_2-RGO upon electrochemical conversion reaction is tracked by *ex situ* XRD and XPS investigation. Fig. 4b exhibits XRD patterns of the FeF_2-RGO at different stages of the first galvanostatic cycling (Fig. 4a). Upon Na^+ reacting with FeF_2-RGO, a new set of peaks appear at $2\theta=39^\circ$ (corresponding to peak of NaF) and 45° (corresponding to peak of Fe), which grow in intensity with the decreases of discharge voltage (1# to 3#) in comparison with the peak of FeF_2 ($2\theta=33^\circ$). When the discharge voltage reaches to 0.8 V (4#), the peaks of FeF_2 almost disappear and only NaF and Fe could be detected, indicating that FeF_2 reacts with Na^+ to generate NaF and Fe. On charging, when the charge voltage increases to 3.0 V (5#), it almost goes through the reverse process. However, it should be noted that even charged to 4.5 V (6#), there are still a lot of residual Fe compared with NaF. It should be noted that the peaks at $2\theta=39^\circ$ (corresponding to peak of Fe_2O_3) are due to oxidation during the preparation of electrode. The XPS spectra of Fe 2p after charging to 3.0 and 4.5 V are illustrated in Figure S3. It is clear that the peak at 713.6 eV, which suggests the +3 oxidation states of iron in the material [48], increases with charge voltage increasing from 3.0 to 4.5 V. In addition, the XPS spectra of Fe 2p after charging to 4.5 V at different cycles are also shown in Figure S4. It can be found that the +3 oxidation states of iron are gradually increasing during cycling, and the amount of +2 oxidation states of iron after 10 cycles is very small. Combining the above results, it could be deduced that the reaction process is as follows:

Initial discharge-charge cycle ($4.5 \geq E \geq 0.8$ V):

Discharge:

$$FeF_2 + 2Na^+ + 2e^- \rightarrow Fe + 2NaF \quad (1)$$

Charge:

$$2NaF + Fe \rightarrow xFeF_2 + yFeF_3 + (1-x-y)Fe + 2Na^+ + 2e^- \ (x+3y/2=1) \quad (2)$$

Intermediate discharge-charge cycles ($4.5 \geq E \geq 1.5$ V):

Discharge:

$$FeF_3 + Na^+ + e^- \rightarrow NaFeF_3 \quad (3)$$

$$FeF_2 \text{ (residual)} + 2Na^+ + 2e^- \rightarrow Fe + 2NaF \quad (4)$$

Charge:

$$2NaF + Fe \rightarrow xFeF_2 + yFeF_3 + (1-x-y)Fe + 2Na^+ + 2e^- \ (x+3y/2=1) \quad (5)$$

$$NaFeF_3 \rightarrow FeF_3 + Na^+ + e^- \quad (6)$$

Finally stable discharge-charge cycles ($4.5 \geq E \geq 1.5$ V):

$$FeF_3 + Na^+ + e^- \leftrightarrow NaFeF_3 \quad (7)$$

The *in situ* generation of the FeF_3-Fe-RGO composite follows the above described gradual transformation of FeF_2 to FeF_3, which is further tracked by the successive cyclic voltammetry (CV) profiles. Figure 3b shows the first CV curve of FeF_2-RGO (0.8-4.5 V), wherein the reduction peak at ca. 1.2 V can be assigned to conversion reaction (Eq. (1)). During the reverse process, the oxidation peaks at ca. 2.3 V can be described by Eq. (2). Interesting, during the successive cycles (1.5-4.5 V), the CV profiles of FeF_2-RGO change gradually. In detail, the reduction/oxidation peaks of conversion reaction of FeF_2 at ca. 1.5 and 2.3 V, respectively, significantly decrease, indicating that the FeF_2 is transformed to FeF_3 gradually. These CV results are consistent with the gradual change in charge/discharge profiles (Fig. 3a). It should be noted that most of the discharge capacity is achieved above 1.7 V, which indicate that it is the Na^+ intercalation reaction mainly responsible for the high capacity. As Fe^{2+} cannot be reduced to Fe^+ and thus Na^+ intercalation into the framework of FeF_2 is impossible, the successful generation of FeF_3 from FeF_2 is thus further confirmed, which is consistent with the proposed reaction process and mechanism mentioned above.

The superior electrochemical performance of the *in situ* generated FeF_3-Fe-RGO composite can be attributed to synergistic effect of the residual Fe and RGO. As the conductive residual Fe is generated accompanied with the generation of FeF_3 from the same FeF_2 grain during electrochemical reaction, the simultaneously generated NaF could

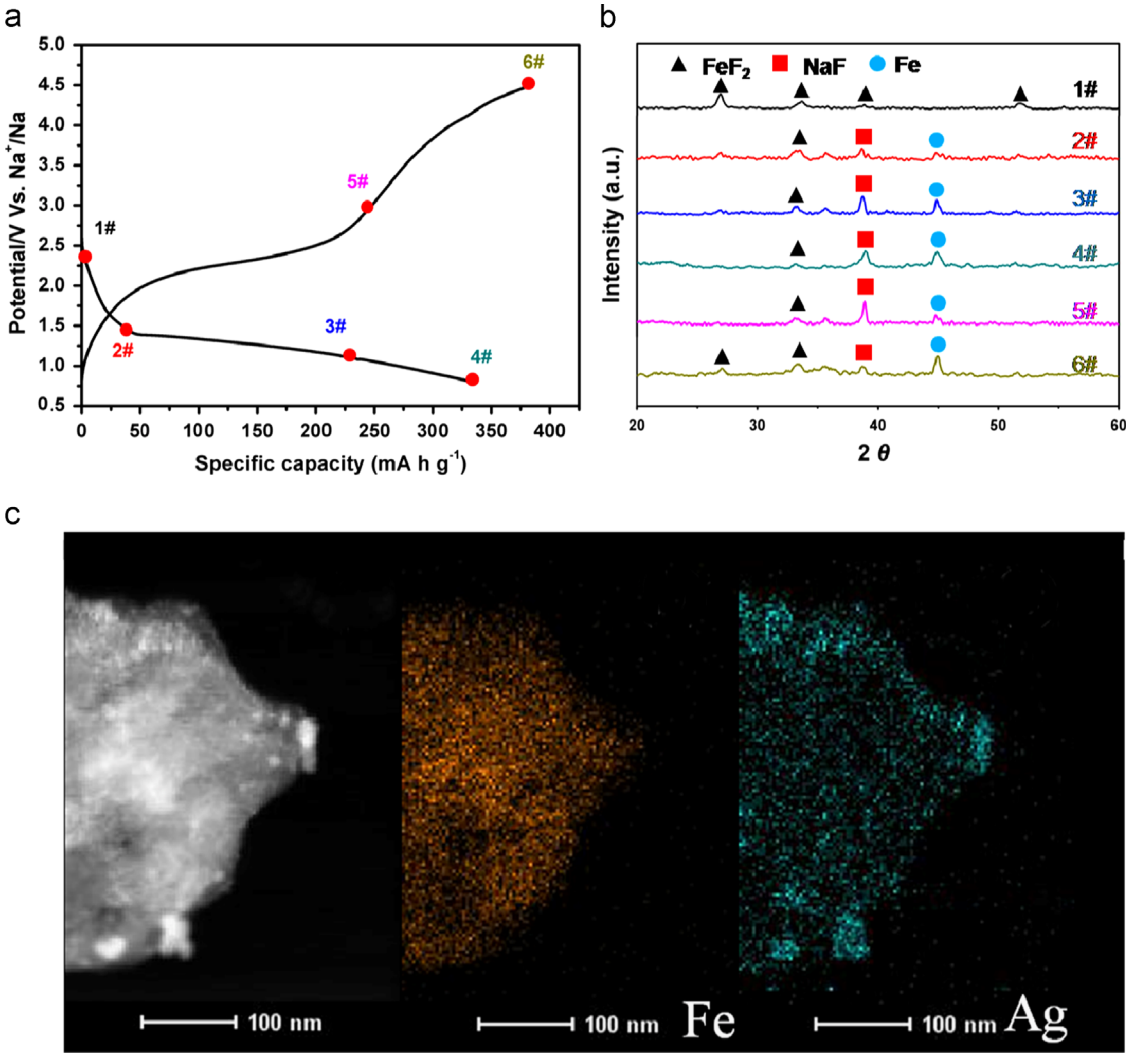

Fig. 4 (a) First discharge–charge profile and (b) the corresponding *ex situ* XRD diffraction patterns recorded at different stages of the galvanostatic cycling of the FeF_2–RGO composite. (c) TEM images and corresponding elemental mapping images of Fe and Ag in the selected area after 50 discharge–charge cycles.

effectively block interparticle Fe diffusion, and, thereby the intrinsically homogeneous distribution of Fe among the FeF_3 matrix could be maintained. As a result, a very effective and homogenous conductive network is formed, which is crucial for enabling highly insulated FeF_3 as feasible cathode materials for NIBs. Considering SEM energy-dispersive X-ray spectroscopy (EDX) technique cannot distinguish the Fe element from metallic Fe and the FeF_3, in order to investigate the distribution of the *in situ* generated residual metallic Fe, a replacement reaction is employed to substitute metallic Fe with Ag for cathode after 50 cycles (see Experimental methods section for details). That is to say, EDX mapping of Ag is employed to reflect the distribution of metallic Fe. As shown in Figure 4c, the sheet-like morphology of the FeF_3–Fe–RGO composite and the homogeneous distribution of the Fe from FeF_3 still remain even after 50 cycles, indicating that the structure is very stable during cycling. Furthermore, it can be seen that Ag uniformly distributes among the matrix, and so does for the metallic Fe. It should be noted that more state-of the-art characterization methods, such as EELS spectra recorded in TEM mode with a spread beam, would be helpful to provide direct evidences of the distribution of Fe in the composite electrode. Consequently, the *in situ* generated and uniformly distributed metallic Fe, as an excellent conductor, would play a key role to enhance the conductivity of FeF_3 formed during electrochemical reaction. For the convenience of understanding, a schematic representation summarizes the above discussed points (Figure 5). Combined with RGO, they can form two dimensionally conductive network to ensure fast and continuous electron transport and prevents the agglomeration of active material during cycling. Moreover, the RGO could act as a buffer matrix to limit the volume variation during charge and discharge cycles. On the contrary, based on the reaction mechanism, there is very limited, if any, residual metallic Fe in the FeF_3-RGO system.

To further prove the efficacy of the *in situ* generated homogeneous Fe matrix toward enhancement of FeF_3, the electrochemical performances of ball milled commercial

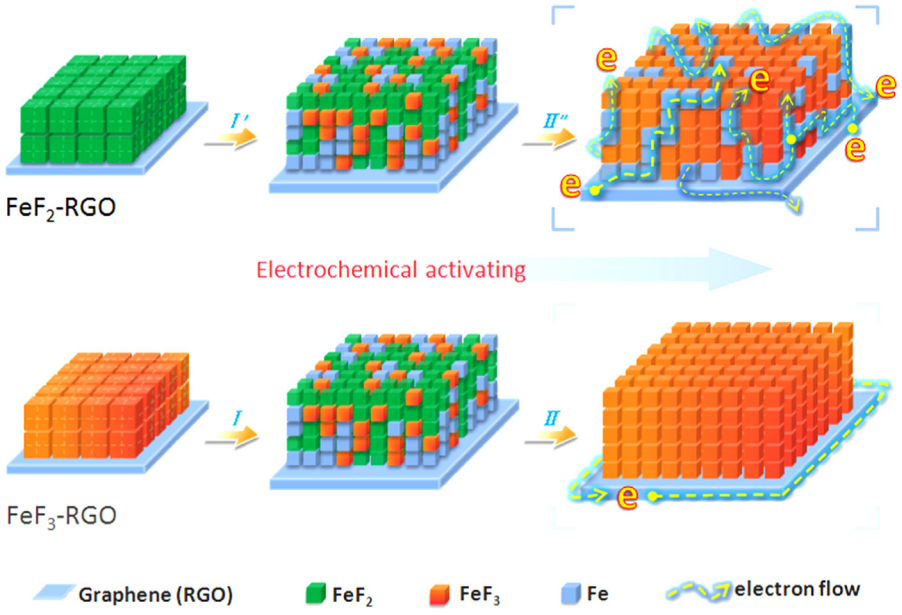

Fig. 5 Schematic summarization and comparison of the electrochemical reaction mechanisms of the FeF_3-RGO and FeF_2-RGO. The *in situ* generated and continuously remained metallic Fe in FeF_3-Fe-RGO composite plays a crucial role in improving the battery performance.

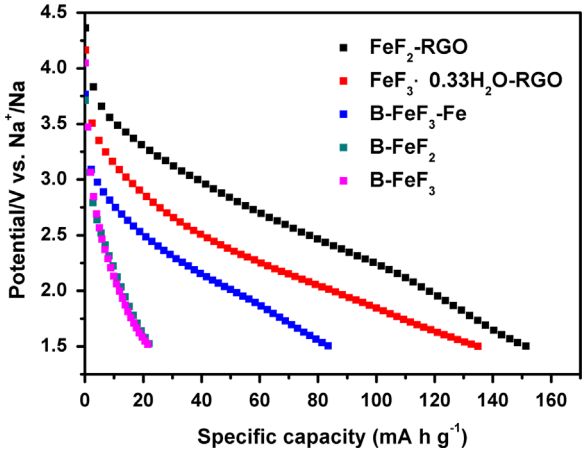

Fig. 6 Comparison of the discharge profiles of the FeF_2-RGO composite and its counterparts (B-FeF_2, B-FeF_3, B-FeF_3-Fe, and $FeF_3 \cdot 0.33H_2O$-RGO) at a current density of 50 mA g^{-1}.

samples including FeF_2, FeF_3, mixture of FeF_3 and Fe, denoted as B-FeF_2, B-FeF_3, B-FeF_3-Fe and $FeF_3 \cdot 0.33H_2O$-RGO, respectively, are also tested for comparison. Fig. S5 shows the XRD patterns of as-prepared samples. It can be seen that the FeF_3 is reduced by the mixed Fe during ball-milling. And some amount of FeF_2 convert into FeF_3 during ball-milling commercial FeF_2 under Ar atmosphere, due to the disproportionation reaction ($Fe^{2+} \rightarrow Fe^0 + Fe^{3+}$). Figure S6 shows the SEM and TEM images of as-prepared samples. Note that for increasing the conductivity of these control samples, more conductive acetylene black is employed than that of FeF_2-RGO during the preparation of the electrode. As shown in Figure 6, compared to FeF_2-RGO, both the discharge capacity (130 mA h g^{-1}) and potential platform of the $FeF_3 \cdot 0.33H_2O$-RGO are much lower, which might be due to the desired homogeneous metallic Fe conductive network cannot be formed for $FeF_3 \cdot 0.33H_2O$-RGO because of its definite proportions of Fe and F (Figure 5 bottom and Figure S9). To further improve the conductivity, FeF_3 is ball milled with the same amount of metallic Fe as in FeF_2-RGO. Although the specific capacity of FeF_3 can be significantly increased from 22 to 82 mA h g^{-1}, it is still much lower than that of FeF_2-RGO, further confirming the importance of our strategy – the Fe should be *in situ* generated. On the other hand, it is found that, even without ball-milling, the specific capacities of both FeF_2-RGO and $FeF_3 \cdot 0.33H_2O$-RGO are much higher than these of their ball milled counterparts (B-FeF_2 and B-FeF_3, respectively), indicating that the RGO could also benefit the battery performance. Figure S7 shows the cycling performance of as-prepared samples. It is clear that FeF_2-RGO exhibits the best cycling performance. The capacity of 100 mA h g^{-1} can be retained after 300 cycles at a current density of 50 mA g^{-1}. All the above results indicate that the enhanced electrochemical activity can be attributed to the synergistic effect of the residual Fe and RGO.

Conclusion

In summary, we have demonstrated a simple while effective method for preparation of the FeF_3-Fe-RGO composite, leading to a double enhancement strategy for highly insulated FeF_3 through *in situ* generated metallic Fe and RGO conductive networks. Superior over previous methods, the key is that the active FeF_3 and conductive Fe are simultaneously *in situ* generated through electrochemical discharge–charge reaction, ensuring their homogenous and intimate contact because the electrochemical reduction takes place from same FeF_2 grain and the mixture could thus be at atomic scale, which is of critical importance for enabling highly insulated FeF_3 as feasible cathode materials for NIBs. The GO not only serves as the template to control the morphology and particle size of the

FeF_3 precursor (FeF_2) but also forms two dimensionally conductive networks after being reduced when it contacts with Fe and FeF_3, which plays a key role to ensure fast and continuous electron and ion transport and also prevents the agglomeration of active material during cycling. As a novel cathode material for NIBs, the composite exhibits superior electrochemical performance including high specific capacity, good rate capability, and long cycling stability. The obtained promising electrochemical results and scientific understanding would provide design principle and encourage more researches for other next generation high-capacity electrode materials while with very low electrical conductivity.

Acknowledgments

This work was financially supported by the 100 Talents Programme of The Chinese Academy of Sciences, the National Program on Key Basic Research Project of China (973 Program, Grant no. 2012CB215500), the fundamental research funds for the central universities, the National Natural Science Foundation of China (Grant nos. 51372007 and 21301014).

Appendix A. Supporting information

Supplementary data associated with this article can be found in the online version at http://dx.doi.org/10.1016/j.nanoen.2014.10.004.

References

[1] J. Tarascon, M. Armand, Nature 451 (2001) 652–657.
[2] D. Yang, Z.Y. Lu, X.H. Rui, et al., Angew. Chem. Int. Ed. 53 (2014) 9352–9355.
[3] H.J. Tang, C.M. Hessel, J.Y. Wang, N.L. Yang, R.B. Yu, H.J. Zhao, D. Wang, Chem. Soc. Rev. 43 (2014) 4281–4299.
[4] Y.P. Du, Z.Y. Yin, X.H. Rui, et al., Nanoscale 5 (2013) 1456–1459.
[5] S.M. Xu, C.M. Hessel, H. Ren, R.B. Yu, Q. Jin, M. Yang, H.J. Zhao, D. Wang, Energy Environ. Sci 27 (2014) 632–637.
[6] Y. Sun, X. Hu, W. Luo, F. Xia, Y. Huang, Adv. Funct. Mater. 23 (2013) 2436–2444.
[7] L. Yu, H.B. Wu, X.W. (David) Lou, Adv. Mater. 25 (2013) 2296–2300.
[8] J.Y. Wang, N.L. Yang, H. Tang, et al., Angew. Chem. Int. Ed. 52 (2013) 5417–6420.
[9] V.L. Chevrier, G. Ceder, J. Electrochem. Soc. 158 (2011) A1011–A1014.
[10] S.W. Kim, D.H. Seo, X. Ma, G. Ceder, K. Kang, Adv. Energy Mater 2 (2012) 710–721.
[11] V. Palomares, P. Serras, I. Villaluenga, K.B. Hueso, J. Carretero-González, T. Rojo, Energy Environ. Sci 5 (2012) 5884–5901.
[12] B.L. Ellis, L.F. Nazar, Curr. Opin. Solid State Mater. Sci 16 (2012) 168–177.
[13] S.P. Ong, V.L. Chevrier, G. Hautier, A. Jain, C. Moore, S. Kim, X. Ma, G. Ceder, Energy Environ. Sci 4 (2011) 3680–3688.
[14] L. Wang, Y. Lu, J. Liu, M. Xu, J. Cheng, D. Zhang, J.B. Goodenough, Angew. Chem. Int. Ed. 52 (2013) 1964–1967.
[15] Z.L. Jian, W.Z. Han, X. Lu, H.X. Yang, Y.S. Hu, J. Zhou, Z.B. Zhou, J.Q. Li, W. Chen, D.F. Chen, L.Q. Chen, Adv. Energy Mater 3 (2012) 156–160.
[16] Y. Park, D.S. Shin, S.H. Woo, N.S. Choi, K.H. Shin, S.M. Oh, K.T. Lee, S.Y. Hong, Adv. Mater. 24 (2012) 3562–3567.
[17] Y. Cao, L. Xiao, M.L. Sushko, W. Wang, B. Schwenzer, J. Xiao, Z. Nie, L.V. Saraf, Z. Yang, J. Liu, Nano Lett. 12 (2012) 3783–3787.
[18] A. Kitajou, H. Komatsu, K. Chihara, I.D. Gocheva, S. Okada, J.I. Yamaki, J. Power Sources 198 (2012) 389–392.
[19] K.H. Ha, S.H. Woo, D. Mok, N.S. Choi, Y. Park, S.M. Oh, Y. Kim, J. Kim, J. Lee, L.F. Nazar, K.T. Lee, Adv. Energy Mater **3** (2013) 770–776.
[20] Y. Yamada, T. Doi, I. Tanaka, S. Okada, J.I. Yamaki, J. Power Sources 196 (2011) 4837–4841.
[21] J. Qian, X. Wu, Y. Cao, X. Ai, H. Yang, Angew. Chem. Int. Ed. 52 (2013) 4633–4636.
[22] F. Badway, F. Cosandey, N. Pereira, G.G. Amatucci, J. Electrochem. Soc. 150 (2003) A1318-A1327.
[23] M.A. Reddy, B. Breitung, V.S.K. Chakravadhanula, C. Wall, M. Engel, C. Kübel, A.K. Powell, H. Hahn, M. Fichtner, Adv. Energy Mater 3 (2012) 308–313.
[24] S.W. Kim, D.H. Seo, H. Gwon, J. Kim, K. Kang, Adv. Mater. 22 (2010) 5260–5264.
[25] L. Li, F. Meng, S. Jin, Nano Lett. 12 (2012) 6030–6037.
[26] C. Li, L. Gu, S. Tsukimoto, P.A. Van Aken, J. Maier, Adv. Mater. 22 (2010) 3650–3654.
[27] C. Li, J. Lin, J. Mater. Chem. 20 (2010) 6831–6847.
[28] F. Wang, H.C. Yu, M.H. Chen, L. Wu, N. Pereira, K. Thornton, A.V. Ven, Y. Zhu, G.G. Amatucci, J. Graetz, Nat. Commun (2012). http://dx.doi.org/10.1038/ncomms2185.
[29] N. Yamakawa, M. Jiang, B. Key, C.P. Grey, J. Am. Chem. Soc. 131 (2009) 10525–10536.
[30] F. Wang, R. Robert, N.A. Chernova, N. Pereira, F. Omenya, F. Badway, X. Hua, M. Ruotolo, R. Zhang, L. Wu, V. Volkov, D. Su, B. Key, M.S. Whittingham, C.P. Grey, G.G. Amatucci, Y. Zhu, J. Graetz, J. Am. Chem. Soc. **133** (2011) 18828–18836.
[31] Y. Ma, S.H. Garofalini, J. Am. Chem. Soc. 134 (2012) 8205–8211.
[32] M. Bervas, F. Badway, L.C. Klein, G.G. Amatucci, Electrochem. Solid-State Lett. 8 (2005) A179-A183.
[33] F. Badway, A.N. Mansour, N. Pereira, J.F. Al-Sharab, F. Cosandey, I. Plitz, G.G. Amatucci, Chem. Mater. 19 (2007) 4129–4141.
[34] X.H. Cao, Y.M. Shi, W.H. Shi, X.H. Rui, Q. Yan, J. Kong, H. Zhang, Small 9 (2013) 3433–3438.
[35] S. Deville, E. Saiz, R.K. Nalla, A.P. Tomsia, Science 311 (2006) 515–518.
[36] L. Estevez, A. Kelarakis, Q. Gong, E.H. Da, E.P. Giannelis, J. Am. Chem. Soc. 133 (2011) 6122–6125.
[37] D.G. Karraker, P.K. Smith, Inorg. Chem. 31 (1992) 1118–1120.
[38] A.P. Grosvenor, B.A. Kobe, M.C. Biesinger, N.S. McIntyre, Surf. Interface Anal 36 (2004) 1564–1574.
[39] X.L. Huang, R.Z. Wang, D. Xu, Z.L. Wang, H.G. Wang, J.J. Xu, Z. Wu, Q.C. Liu, Y. Zhang, X.B. Zhang, Adv. Funct. Mater. 23 (2013) 4345–4353.
[40] S. Stankovich, D.A. Dikin, R.D. Piner, K.A. Kohlhaas, A. Kleinhammes, Y. Jia, Y. Wu, S.T. Nguyen, R.S. Ruoff, Carbon 45 (2007) 1558–1565.
[41] J. Chen, K. Sheng, P. Luo, C. Li, G. Shi, Adv. Mater. 24 (2012) 4569–4573.
[42] J.Q. Liu, Z.Y. Yin, X.H. Cao, F. Zhao, L.H. Wang, W. Huang, H. Zhang, Adv. Mater. 25 (2013) 233–238.
[43] X. Huang, Z. Yin, S. Wu, X. Qi, Q. He, Q. Zhang, Q. Yan, F. Boey, H. Zhang, Small 7 (2011) 1876–1902.
[44] Q. He, H.G. Sudibya, Z. Yin, S. Wu, H. Li, F. Boey, W. Huang, P. Chen, H. Zhang, ACS Nano 4 (2010) 3201–3208.
[45] X. Huang, X. Qi, F. Boey, H. Zhang, Chem. Soc. Rev. 41 (2012) 666–686.
[46] L. Li, Y. Yu, F. Meng, Y. Tan, R.J. Hamers, S. Jin, Nano Lett. 12 (2012) 724–731.
[47] J.B. Goodenough, Y. Kim, Chem. Mater. 22 (2010) 587–603.
[48] L. Liu, M. Zhou, L. Yi, H. Guo, J. Tan, H. Shu, X. Yang, Z. Yang, X. Wang, J. Mater. Chem. 22 (2012) 17539–17550.

Delong Ma reveived his Bachelor's degree in Jilin university in 2009. He then joined research group of Prof. Zhanyi Cao at Jilin university for Ph.D. study. He is currently working on design and synthesis of nanomaterials for Li-ion and Na-ion batteries.

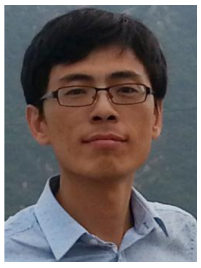

Heng-guo Wang received his Ph.D. degree in 2011 from Jilin University. From 2011 to 2013, he stayed in Changchun Institute of Applied Chemistry as a Postdoctoral Research Associate. Currently Dr. Wang is an Associate Professor at School of Materials Science and Engineering in Changchun University of Science and Technology. His research interests include nanomaterials and their application in energy storage and conversion fields, such as lithium ion batteries, sodium ion batteries, and supercapacitors.

Yang Li studied at the school of chemistry and chemistry engineering, South China University of Technology (SCUT) and got the Bachelor degree in 2011. Then he received a Master degree in chemistry in the School of Chemistry and Environment, Beihang University (BUAA) in 2014. From 2011 to now, under the direction of Professor Zhang Yu, his work centers on the design and synthesis of nanostructure materials with controllable properties.

Dr. **Dan Xu** received her B.S. and Ph.D. degrees in applied chemistry from Jilin University, China, in 2005 and 2010, respectively. She then went to the Changchun Institute of Applied Chemistry (CIAC), Chinese Academy of Sciences (CAS) working as a postdoctor from 2011 to 2013. As of 2013, she is working as an Assistant Professor under the direction of Prof. Xin-Bo Zhang at CIAC, CAS. Her current research interests include the characterization of electrolytes and catalysts as well as the mecha-nism analysis of Li–O2 batteries via in situ methods.

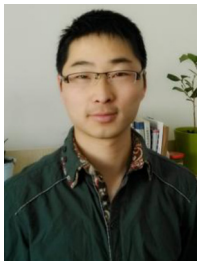

Shuang Yuan received his Master degree in Condensed Matter Physics from Northeastern University of China, in 2012. He is currently pursuing his Ph.D. in Inorganic Chemistry at Changchun Institute of Applied Chemistry (CIAC), Chinese Academy of Sciences (CAS) and Materials Science at Jilin University of China, under the supervision of Prof. Xin-bo Zhang and Prof. Yong-bing Liu. His current interests include the synthesis and characterization of nanostructures, especially transition-metal oxides and their energy-related application for energy storage and conversion.

Xiao-lei Huang received his Ph.D. degree in 2013 from University of Chinese Academy of Sciences, Changchun Institute of Applied Chemistry (CIAC). Currently, he stays in National University of Singapore as a Postdoctoral. His research interests include nanomaterials and their application in energy storage, such lithium ion batteries, sodium ion batteries, and water-splitting for hydrogen production.

Dr. **Xinbo Zhang** (1978) joined Changchun Institute of Applied Chemistry (CIAC) as a professor of "Hundred Talents Program" of Chinese Academy of Sciences (CAS) in the spring of 2010. He received his Ph.D. degree in inorganic chemistry from CIAC and was granted the CAS Presidential Scholarship Award in 2005. Then, during 2005–2010, he worked as a JSPS and NEDO fellow at National Institute of National Institute of Advanced Industrial Science and Technology (Kansai Center), Japan. His interests mainly focus on functional inorganic materials for energy storage & conversion with fuel cells and batteries, especially lithium-air batters.

Dr. **Yu Zhang** received his Doctor degree in Chemistry from Jilin University in 2007. Then, he worked as a new energy and industrial technology development organization (NEDO) fellow at Hiroshima University, Japan. Since March 2013, he joined Beihang University as a "Zhuoyue" program Associate Professor. His interests mainly focus on advanced materials for hydrogen storage, lithium/sodium ion battery, and fuel cells.